IEEE Access
Multidisciplinary ⋮ Rapid Review ⋮ Open Access Journal

Received 7 August 2024, accepted 4 September 2024, date of publication 9 September 2024, date of current version 27 September 2024.

Digital Object Identifier 10.1109/ACCESS.2024.3456106

RESEARCH ARTICLE

The Impedance Calculating Method of Steel Mill Short Net Conductors Based on Finite Element Method

QIAO MA[1,2], (Member, IEEE), BING TONG[1], XIANGQIAN TONG[2], TENG ZHAO[1], YADAN SHANG[1], FENGHUI ZHAO[1], AND DONG ZHANG[1]

[1]China National Heavy Machinery Research Institute Company Ltd., Xi'an 710018, China
[2]School of Automation and Information Engineering, Xi'an University of Technology, Xi'an 710048, China

Corresponding author: Bing Tong (Tongbing1125@163.com)

ABSTRACT The short net is a high-current system with complex geometric shapes in electric furnace steelmaking. The short net impedance calculation is a necessary foundation and basis for designing short net parameters. Traditional analytical methods can difficultly calculate the impedance of short net conductors with complex geometric models. Considering the skin and proximity effects, this paper proposes a finite element method (FEM) based impedance calculation method for short net conductors. Firstly, a frequency domain model of the electromagnetic field is established, and boundary conditions are provided. Then, the FEM based on the Galerkin weighted residual method is used to discretize the established electromagnetic field differential equations. Finally, the short net conductors of a 100-ton electric furnace are taken as the rest. The results show that sudden current density change caused by cross-section change in copper tubes and conductive arms is dramatic. The difference in AC and DC resistance between copper tubes, water-cooled cables, and conductive arms is significant.

INDEX TERMS Short net conductors, electromagnetic field, finite element method, current density, impedance calculation.

I. INTRODUCTION

With the intensification of the environmental crisis, energy saving and emission reduction technologies in various industries have been a concerned. As a pillar industry in essential fields such as people's livelihood, military and aerospace, the steel industry has been developing in a green and low-carbon direction. Compared with the traditional converter steelmaking process, the electric furnace steelmaking process can reduce energy by 60% and emissions by 80% [1]. However, the electric power consumption of the electric furnace steelmaking process is huge, and the power consumption per ton of steel is 400 to 600 kWh [2]. As an important carrier of electric furnace power supply, the short net system carries current up to 50,000-80,000 amps [3]. The short net system refers to the conductive equipment between the low-voltage side of the transformer and the molten steel. It is composed of four parts: copper tubes, water-cooled cables, conductive arms and graphite electrodes. The design of the short net system has a great influence on the energy consumption in electric furnace steelmaking process. The complicated geometric shape and strong electromagnetic field interference exist in short net conductors, which causes the short net conductors impedance calculation to be difficult. However, the impedance calculation is significant for the optimization design of the short net system.

Scholars recognized the difference between DC and AC impedance and inductance long ago. The current density of the conductor shows an uneven distribution under AC conditions, which changes the ability of the conductor to transmit current and thus changes the resistance. The impedance calculation of the short net conductors is closely related to the electricity consumption in steel mills. However, compared to the construction costs of billions, the benefits of electricity consumption (hundreds of thousands or even millions) are too small to attract the attention of steel mills' homeowners. The mechanical and electrical designers often

The associate editor coordinating the review of this manuscript and approving it for publication was Lei Zhao.

overlook the skin and proximity effects of conductors, taking the DC impedance instead of the AC impedance. In order to improve the operational efficiency of steel mills and reduce system energy consumption, it is necessary to study the calculation method of short net impedance for steel mills, considering the effects of skin and proximity.

The geometric mean distance method (GMD) was representative of early impedance calculation methods for the short net conductors [4], [5], [6]. To calculate the impedance of the high-current air-insulated bus duct system between the generator and step-up transformer, [4] uses an improved computation model based on the GMD method. Applying the GMD of rectangular areas to the magnetic potential, [5] proposes a novel computation model to compute the leakage reactance of step lap-core power transformers. To analyze the inductance gradient in electromagnetic rail launchers, [6] establishes an analytical model of the time-varying inductance gradient based on the GMD idea. The GMD method can give the impedance of the conductors with simple geometric. However, some important issues are always ignored, such as the conductor's uneven distribution of current density when passing through alternating current, which causes an inaccurate impedance calculation result.

According to Maxwell's electromagnetic field theory, the skin effect [7] and proximity effect [8] exist in three-phase conductors passing through alternating current. The skin and proximity effects can change the current density distribution within the conductor, further affecting the conductors' AC impedance. Therefore, many scholars have proposed conductor impedance calculation methods considering skin and proximity effects [9], [10], [11]. Reference [9] establishes an analytical model that considers skin and proximity effects to investigate the coupling through a hollow shield of twinax cables. The effects of the nonuniformities and cable geometry deformation on the cable transmission speed are investigated in [10], which considers the skin and proximity effects with high frequency. To obtain the AC copper loss of high-speed permanent magnet machines, [11] establishes the model of the eddy current field considering the skin effect and the proximity effect for form-wound windings. The methods proposed in the above literature can provide an impedance to irregular cross-section conductors, considering skin and proximity effects. Since the skin and proximity effect coefficients are closely related to the geometric shape of conductors, calculating the coefficient is very difficult for conductors with complex geometric models. Therefore, the numerical method is critical in solving impedance for conductors with complex models.

The uneven distribution of current density inside the short net conductors is mainly caused by the interaction of electromagnetic fields between phases. Hence, it is necessary to establish a reasonable impedance model starting from the basic principles of electromagnetic fields. The finite element method (FEM) is a mainstream numerical solution algorithm for electromagnetic field boundary value problems [12], [13]. Reference [14] uses the FEM to solve the stray loss of components in the time-varying magnetic field. The influence of the shell structure and the shell material on the shell eddy current loss is studied based on the FEM in [15]. Reference [16] develops an improved numerical method for resolving the low-frequency breakdown anomaly in the traditional FEM. Reference [17] proposes a FEM-based 3D thermal analysis method for cable joints, considering the impacts of external electromagnetic fields. These works pay attention to the solving of electromagnetic fields in various situations. However, it has not yet been seen to apply the FEM to the impedance calculation of short net conductors in electric furnace steel plants.

Traditional analytical methods are difficult to adapt to the impedance calculation of the short net conductors. This paper proposes an impedance calculating method based on FEM for the short net conductors accounting for both the skin and proximity effects, which has not been found in other papers. Firstly, a frequency domain mathematical electromagnetic field model is established, and boundary conditions are given. Furtherly, the FEM based on the Galerkin weighted margin method is used to discretize the frequency domain equations of the electromagnetic field. Finally, taking the short net conductors corresponding to a 100-ton electric arc furnace as a test object, the conductors' current density and impedance calculation results are presented. The main contribution can be stated as follows:

(1) This paper proposes an impedance calculation method for the short net conductors based on FEM, which is not limited by the geometric model of conductors. The impedance of irregular conductors with large dimensions and small cross-sections can be calculated in particular.

(2) The proposed method can provide the current density at any point in the conductor, which can be used to analyze the relationship between skin and proximity effects and the conductor's' geometric shape.

The rest of this paper is organized as follows: Section II gives the frequency domain equations of the electromagnetic field and boundary conditions. Section III gives the FEM-based solving model of established electromagnetic field equations. Section IV analyzes the impedance calculation results for a real short net system, and Section V gives the conclusion.

II. THE MATHEMATICAL MODEL OF TIME-VARYING ELECTROMAGNETIC FIELD

The electric heating system in the steel mill operates at a power frequency of 50 Hz. The skin and proximity effects will cause the uneven distribution of current density in the short net conductors. To analyze the short net conductor's current density distribution and AC impedance, it is necessary to establish a three-dimensional electromagnetic field mathematical model in the frequency domain. In this section, the electromagnetic field mathematical model in the frequency domain is derived, and the corresponding boundary conditions are given in terms of the theory of time-varying electromagnetic field.

A. THE ELECTROMAGNETIC FIELD FUNDAMENTAL EQUATIONS

The complex form of Maxwell's electromagnetic induction equations can be expressed as [18]:

$$\begin{cases} \nabla \times \boldsymbol{H} = j\omega \boldsymbol{D} + \boldsymbol{J} \\ \nabla \times \boldsymbol{E} = -j\omega \boldsymbol{B} \\ \nabla \cdot \boldsymbol{B} = 0 \\ \nabla \cdot \boldsymbol{D} = \rho \end{cases} \tag{1}$$

where $\boldsymbol{H}$, $\boldsymbol{E}$, $\boldsymbol{B}$, $\boldsymbol{D}$ represent the magnetic field intensity, electric field intensity, magnetic induction intensity and electric induction intensity, respectively. $\boldsymbol{J}$ is the current source. ρ is the space charge density.

The following relationships, integral to the understanding of the Maxwell electromagnetic induction equations, are also satisfied between variables.

$$\begin{cases} \boldsymbol{D} = \varepsilon \boldsymbol{E} \\ \boldsymbol{B} = \mu \boldsymbol{H} \\ \boldsymbol{J} = \sigma \boldsymbol{E} \end{cases} \tag{2}$$

where ε, μ and σ represent permittivity, relative permeability and electrical conductivity, respectively.

According to the basic principles of electromagnetism, $\boldsymbol{E}$ and $\boldsymbol{B}$ can be represented by vector magnetic potential $\boldsymbol{A}$ and scalar electrical potential φ, respectively.

$$\begin{cases} \boldsymbol{E} = -\nabla \varphi - j\omega \boldsymbol{A} \\ \boldsymbol{B} = \nabla \times \boldsymbol{A} \end{cases} \tag{3}$$

where ω is the angular velocity corresponding to the frequency of the field source.

Based on (1) and (3), the frequency domain equation of the electromagnetic field can be expressed as:

$$\begin{cases} \dfrac{1}{\mu} \nabla \times \nabla \times \boldsymbol{A} + \sigma \left(j\omega \boldsymbol{A} + \nabla \varphi \right) = \boldsymbol{J} \\ \nabla \cdot \sigma \left(\omega \boldsymbol{A} + \nabla \varphi \right) = 0 \end{cases} \tag{4}$$

When the spatial current source $\boldsymbol{J}$ and the conductivity σ are known, $\boldsymbol{A}$ and φ can be obtained by equation (4), and then $\boldsymbol{E}$ and $\boldsymbol{B}$ can be obtained.

B. THE ELECTRIOMAGNETIC FIELD BOUNDARY CONDITIONS

The schematic diagram of boundary conditions is shown in Fig. 1. At the interface of different conductivity areas, the boundary conditions can be stated as:

$$\begin{cases} \dfrac{\boldsymbol{e}_n}{\mu} \times \left(\nabla \times \boldsymbol{A}_1 - \nabla \times \boldsymbol{A}_2 \right) = 0 \\ \boldsymbol{e}_n \cdot \sigma_1 \left(j\omega \boldsymbol{A}_1 + \nabla \varphi_1 \right) - \boldsymbol{e}_n \cdot \sigma_2 \left(j\omega \boldsymbol{A}_2 + \nabla \varphi_2 \right) = 0 \\ \boldsymbol{A}_1 - \boldsymbol{A}_2 = 0 \\ \varphi_1 - \varphi_2 = 0 \end{cases} \tag{5}$$

where $\boldsymbol{e}_n$ is the standard unit vector at the interface of regions 1 and 2, with the direction from region 1 to region 2.

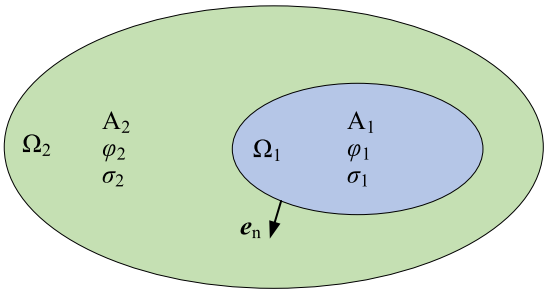

FIGURE 1. The schematic diagram of boundary conditions.

At the interface between adjacent conductivity regions, the magnetic and electrical potential on both sides is equal and opposite in sign. They sum and cancel each other out. In particular, the conductivity is zero at the interface between air and conductor. According to the continuity theorem of current, the boundary conditions can be simplified:

$$\boldsymbol{e}_n \cdot \sigma \left(j\omega \boldsymbol{A} + \nabla \varphi \right) = 0 \tag{6}$$

III. THE ELECTROMAGNETIC FIELD MODEL SOLVING BASED ON FEM

Generally, due to the coupling of electric and magnetic fields and the complexity of conductor geometry models, solving (4) directly is difficult. The FEM is an efficient numerical method for solving the boundary value problems of partial differential equations. The solution domain is considered to be composed of many small interconnected subdomains called finite elements. A suitable (relatively simple) approximate solution is assumed for each subdomain. Then, it is deduced that the overall conditions for solving this domain are satisfied to obtain the problem's solution. This section adopts the Galerkin weighted margin method of FEM to discretize the electromagnetic field equations, and the solving flow is given.

A. THE DIFFERENTIAL EQUATIONS SOLVING

After obtaining the electromagnetic field frequency domain equations, it is necessary to discretize (4). There are two main finite element discretization methods: the Galerkin weighted margin method and the Ritz variational method. In this paper, the most commonly used Galerkin weighted residual method is chosen to discretize the equations. The existing studies show that the results obtained by using vector and scalar weight functions in Galerkin discretization are identical. Then, the vector weight function is used to discretize the equation [19].

$$\int_{\mathrm{V}} \boldsymbol{w} \cdot \frac{1}{\mu} \left(\nabla \times \nabla \times \boldsymbol{A} \right) \mathrm{d}\Omega + \int_{\mathrm{V}} \boldsymbol{w} \cdot \left(j\omega\sigma \boldsymbol{A} + \sigma \nabla \varphi \right) \mathrm{d}\Omega = \boldsymbol{J} \tag{7}$$

$$\int_{\mathrm{V}} \boldsymbol{w} \cdot \nabla \cdot \left(j\omega\sigma \boldsymbol{A} + \sigma \nabla \varphi \right) \mathrm{d}\Omega = 0 \tag{8}$$

where V is the solution domain.

The vector Green's first formula is used for (7):

$$\int_V \frac{1}{\mu}(\nabla \times \boldsymbol{w} \cdot \nabla \times \boldsymbol{A})\,\mathrm{d}\Omega - \oint_S \frac{1}{\mu}\boldsymbol{w} \cdot (\boldsymbol{e}_n \times \nabla \times \boldsymbol{A})\,\mathrm{dS} + \int_V \boldsymbol{w} \cdot (j\omega\sigma\boldsymbol{A} + \sigma\nabla\varphi)\,\mathrm{d}\Omega = 0 \quad (9)$$

where S is the interface between different conductivity regions.

After performing the operator operation, (8) can be rewrite as:

$$\int_V \nabla\boldsymbol{w} \cdot (j\omega\sigma\boldsymbol{A} + \sigma\nabla\varphi)\,\mathrm{d}\Omega - \oint_S \boldsymbol{w} \cdot (j\omega\sigma\boldsymbol{A} + \sigma\nabla\varphi) \cdot \boldsymbol{e}_n \mathrm{dS} = 0 \quad (10)$$

The approximate solutions are obtained by solving the approximate functions, which are formed by combining the essential and interpolation functions [20].

$$\boldsymbol{A} = \sum_{i=1}^{n} N_i \boldsymbol{A}_i \quad (11)$$

$$\varphi = \sum_{i=1}^{n} N_i \varphi_i \quad (12)$$

where N_i is the interpolation function in each small cell. i is the small cell number. n is the total number of the small cell. $\boldsymbol{A}_i$ and φ_i are magnetic and scalar potential in the i-th small cell, respectively.

After substituting the approximate functions into (9) and (10), the discretized electromagnetic field frequency domain equations are obtained. Finally, $\boldsymbol{A}$ and φ of all subdomains can be calculated, then $\boldsymbol{E}$ and $\boldsymbol{B}$ are obtained.

B. THE SOLVING STEPS OF FEM

The solving flow chart is shown in Fig. 2. Firstly, the electromagnetic field differential equation and the boundary condition should be established. Secondly, the differential equation discretization approach needs to be determined. Finally, the matrix discretization equations are solved, and the calculation results are given.

IV. CALCULATION RESULTS ANALYSIS

A 100 tons of electric arc furnace is taken as an example. The power supply transformer parameters are as follows: the primary side voltage is 35 kV, the rated capacity is 90 MVA, and the secondary side rated current is 72000 A. The overall model of the short net is shown in Fig. 3. The geometrical dimension is 15.76 × 3.59×13.75 m. The FEM simulation results are obtained based on the Ansys software. The short net conductors consist of four parts: copper tubes, water-cooled cables, conductive arms, and graphite electrodes. The head end of the copper tubes is connected to the transformer's low-voltage terminal. The graphite electrodes breakdown the air to form a current loop with the scrap steel to melt the steel in the ladle car. Due to the limited computer memory, the model has to be calculated in four parts. Fig. 4 shows the diagram of the model out boundary and current source distribution. The current source is implemented by selecting the current inflow and outflow surfaces in the coil module of the software. All domains satisfy Ampere's law, and all boundaries meet magnetic insulation. In this section, the current density distribution of each part for the short net conductors is analyzed, whereas the AC and DC impedance of each part is compared.

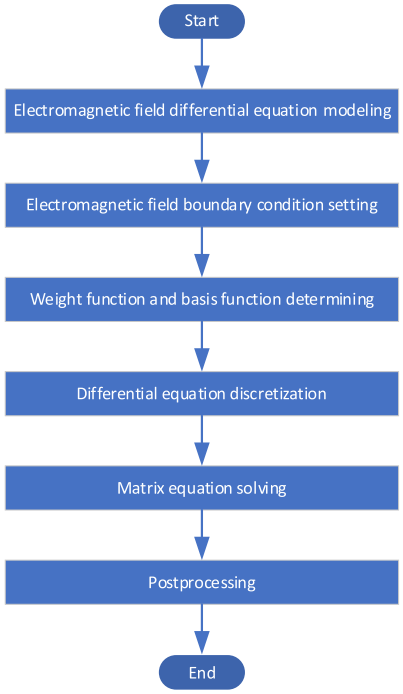

FIGURE 2. The solving flow chart of FEM.

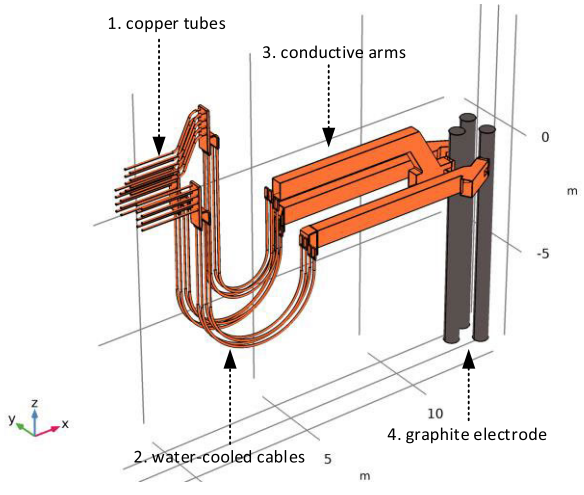

FIGURE 3. The overall model of the short net conductors.

A. COPPER TUBES

The single phase copper tube comprises eight slender copper tubes and a copper busbar. The dimensions of copper tubes

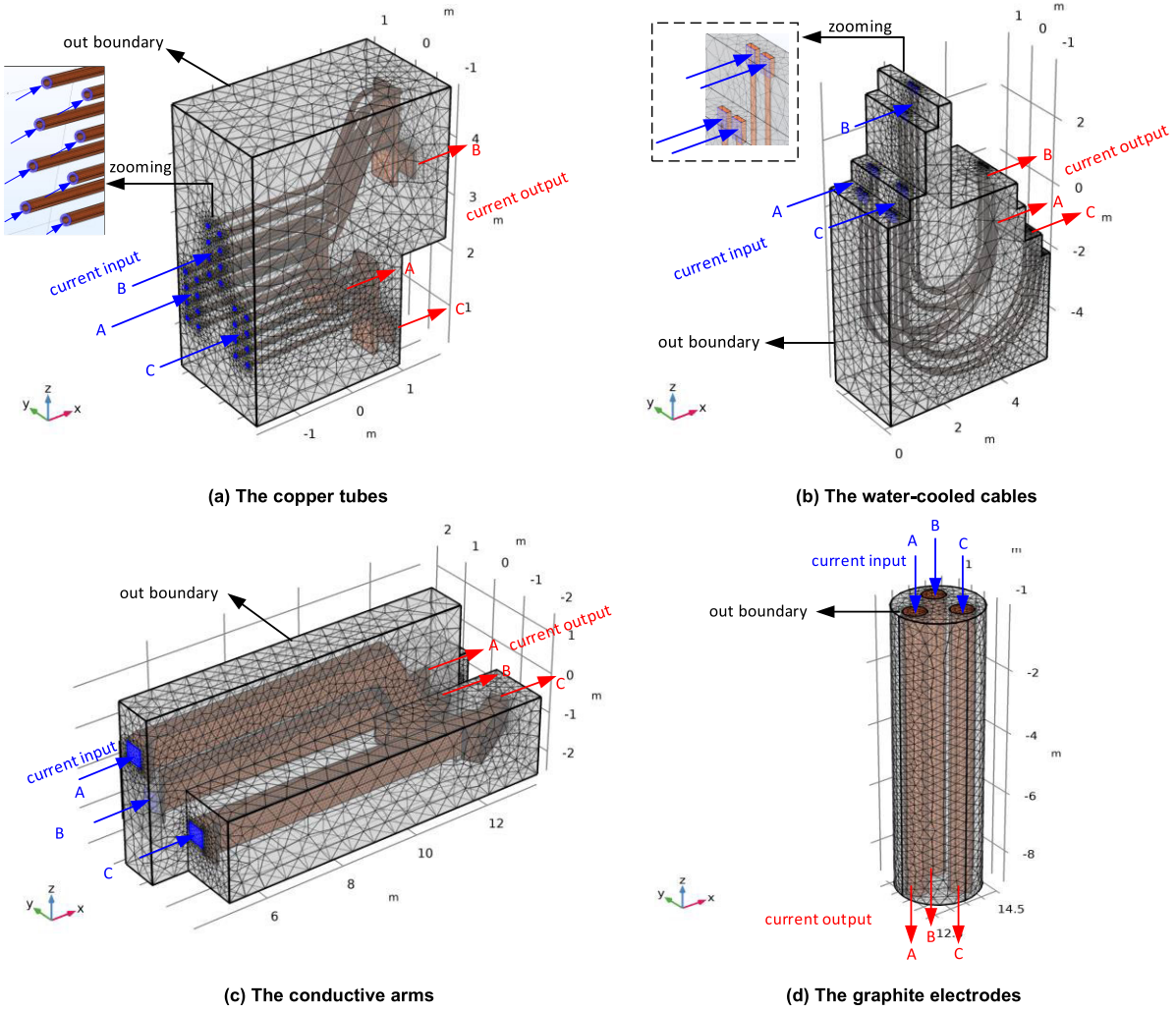

FIGURE 4. The diagram of the out model boundary and current source distribution.

and busbar can be seen in Fig. 4. Since the copper tubes are hollow conductors with a certain thickness, the dimensions are depicted with thickness and length. The radius of the copper tubes is 25 mm (small radius) and 40 mm (large radius). The dimensions of phase B and phase AC are 15 × 4474 mm and 15 × 3000 mm, respectively. The dimensions of the copper busbar are 500 × 1630×90 mm (vertical part) and 500 × 789×48 mm (curved part), respectively. The current input and output terminals are copper tubes and busbar, and the direction is the x-axis.

1) CURRENT DENSITY DISTRIBUTION

Fig. 5 gives the surface current density of copper tubes. It can be easily found that the areas with high amplitude of current density are concentrated at the intersection of the copper busbar. The maximum current density is 3.13 × 103 A/mm^2. The farther away from the copper busbar, the lower the current density of the copper tube. The cross area of the vertical and curved copper busbar is 7750 cm^2 and 240 cm^2. The difference in values between the two is over 30 times, which causes the conductivity sudden change at the intersection. The great change of conductivity causes the current density change obviously. Specifically, the change degree and range of smaller cross sections' conductors are greater than those of larger cross sections. The high current density mainly exists in the curve copper busbar.

The current density slice diagram of copper tubes is shown in Fig. 6, and each copper tube is numbered. Overall, the current density distribution is not uniform. However, the difference in radial current density of conductors is slight. The skin and proximate effect in copper tubes is insignificant, which is closely related to the geometry shape of the conductor. The ratio of thickness to radius of the copper conductor is small, with 0.375, resulting in a weak skin effect. The ratio of radius to spacing of the copper conductor is low at 0.13, which weakens the proximity effect.

Fig. 7 gives the current density of different copper tubes. It can be seen that the current density of A8, B8, and C8 has a significant increase at the end part. However, the current density of A1 and C1 is always very small, whereas the value

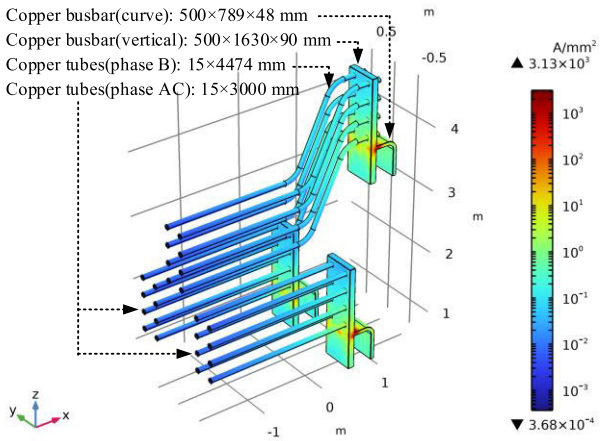

FIGURE 5. The surface current density of the copper tubes.

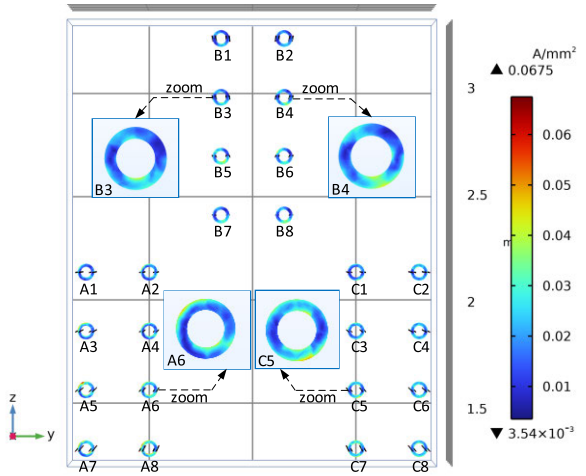

FIGURE 6. The current density slice diagram at x=-1m of the copper tubes.

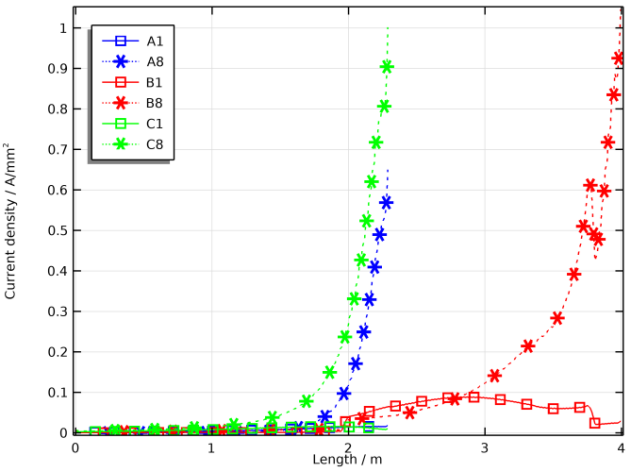

FIGURE 7. The current density of the different copper tubes.

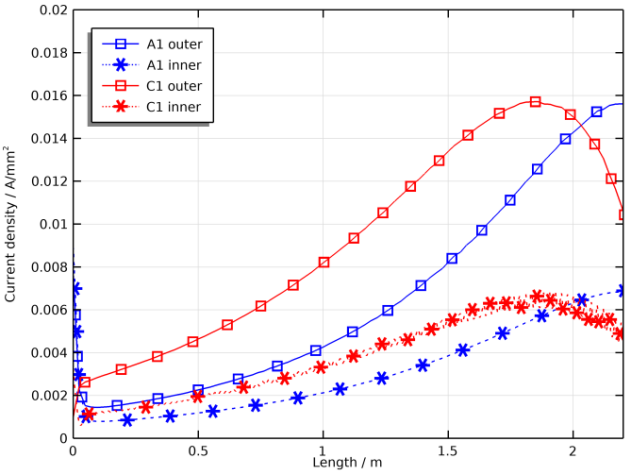

FIGURE 8. The current density of the tube's inner and outer wall.

of B1 increases slightly in the latter part. The reason is that A8, B8, and C8 are connected at the low position of the copper busbar, which is affected dramatically by the current density sudden change by the copper busbar. Similarly, A1, B1, and C1 located in the upper part of the copper busbar are less affected, which cause arelatively stable current density.

Fig. 8 gives the current density distribution of the inner and outer wall of copper tube A1 and C1. It can be found that the current density of the outer wall is higher than the inner wall. Although the skin effect works weak from Fig. 4, the influence still exists in the conductor. According to the theory of electromagnetic wave propagation, the current in an AC system is more concentrated on the surface of the conductor. Therefore, the outer wall has a high current density compared with the inner wall.

2) IMPEDANCE CALCULATION RESULTS

The impedance calculation results of copper tubes are shown in Table 1. The DC and AC resistance of the three phases are 1.99, 3.04, 1.99 uΩ, and 7.54, 9.98, 7.54 uΩ, respectively. Compared with DC values, the AC values increase by 279%, 228%, and 279%, respectively. The DC and AC inductance of the three phases is 0.73, 1.42, 0.73 uΩ, and 0.61, 1.28, 0.61 uΩ, respectively. Compared with DC values, the AC values decreased by 16%, 10%, and 16%, respectively. The AC reactance of the three phases is 189.42, 401.71, 189.45 uΩ, respectively. The imbalance of the three-phase imbalance index [21] is about 54%, mainly determined by inductance. The results indicate a significant difference in resistance between AC and DC, a relatively small difference in inductance, and a high degree of three-phase impedance imbalance.

TABLE 1. The impedance of the copper tubes.

	frequency/Hz	A-phase	B-phase	C-phase
resistance/uΩ	0	1.99	3.04	1.99
	50	7.54	9.98	7.54
inductance/uH	0	0.73	1.42	0.73
	50	0.61	1.28	0.61
reactance/uΩ	50	189.42	401.71	189.45

B. WATER-COOLED CABLES

The water-cooled cables are located in the second part of the short net conductors. The head and tail end are connected with

the copper tubes and the conductive arms, respectively. The single-phase water-cooled cable consists of four independent parallel cables. Each cable's length and radius are 11.5 meters and 3.9 centimeters, respectively.

1) CURRENT DENSITY DISTRIBUTION

Fig. 9 gives the surface current density of the water-cooled cables. It can be found that the current density has a great uneven distribution with the large value at the middle-curved part and small value at the two ends. The maximum current density is 36.1 A/mm^2. After regarding the all cables as a whole conductor, the current density is high in the edge area and small in the center area.

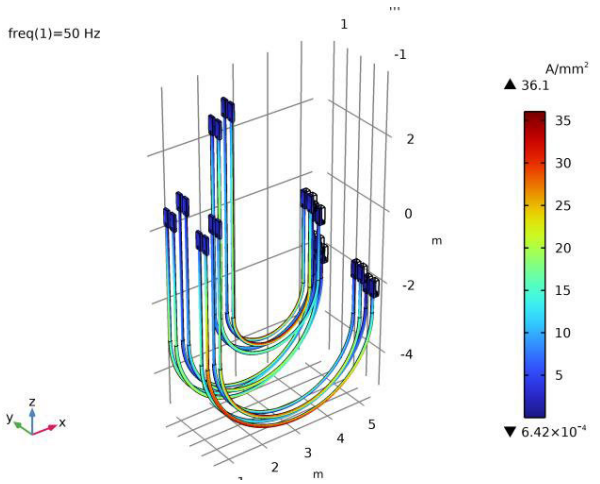

FIGURE 9. The surface current density of water-cooled cables.

Fig. 10 is a current density slice diagram. The maximum current density of cables numbered from A1 to A4 is 31.95, 25.91, 34.66 and 25.86 A/mm^2, respectively. The cable numbered A3 has the highest current density, followed by A1, and A2 and A4. The reason is that the electromagnetic field generated by the B and C phase affects the current density of A phase cables, and the influence degree is related to the cable position. According to the basic principle of electromagnetic field, the proximity effect exists between the parallel conductors. Specifically, when the current direction is the same for the two conductors, the edge position has a high current density, and the center position has a low. Cable numbered A3 has the strongest edge properties, resulting in the highest A3 current density. From B1 to B4, the maximum current density is 35.51, 35.41, 23.11 and 23.81 A/mm^2, respectively. It can be found that the current density of B1 and B2 is larger, while B3 and B4 are smaller. Besides, the current density distribution of phase C cables is similar to phase A. The cable numbered C4 has the strongest edge properties and the highest current density at 34.41 A/mm^2.

Fig. 11 gives the current density distribution of the four cables with the high average current densities. The distribution law of current density is obvious. A3 and C4 cables are geometrically symmetrical, so that the current density distribution of the two cables is almost the same. The mean current densities of the two are 11.83 and 11.79 A/mm^2, respectively. B1 and B2 cables are also geometrically symmetrical, with average current densities of 15.29 and 15.30 A/mm^2, respectively. The current density of the B phase is higher than that of the A and C phases, which is related to the spatial layout of the cable. As can be seen from the overlooking angle of Fig. 7, the four cables of phase B are parallel to the X-axis. However, both phase A and C cables have a certain angle with the X-axis, and there are two parallel structures in the four cables. Cable 1 is parallel to cable 2, and cable 3 is parallel to cable 4. Accordingly, compared with phase B of parallel structure, the incomplete parallel structure of A and C phase cables has a reduction influence on the current density.

Fig. 12 gives the current density at the top and bottom of the curved part for A2 and A3 water-cooled cables. It can be found that the current density at the top and bottom of the cable is quite different. The bottom of the A3 cable has the highest current density, followed by the top of A2 and A3. the bottom of A2. The average current density at the bottom of A3 is about 11.83 A/mm^2, which is 1.3 times that at the top. The average current density at A2 top is about 9.82 A/mm^2, 3.2 times that at the bottom. From the above analysis, the current density distribution at different cable positions is enormously different. From a global perspective of the three phases, due to the strong edge properties, the current density at A3 bottom with the most edge properties is the highest. Similarly, the current density at A2 bottom with most center properties is lowest.

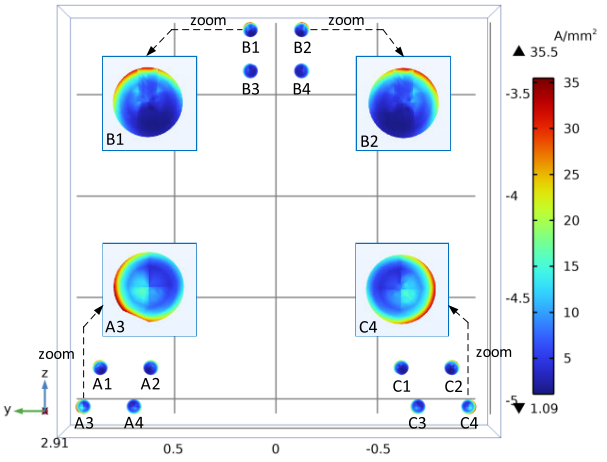

FIGURE 10. The cables current density slice diagram at x=3 m.

2) IMPEDANCE CALCULATION RESULTS

The impedance calculation results of the water-cooled cables are shown in Table 2. The DC and AC resistance of the three phases are 14.28, 28.13, 14.39 uΩ, and 42.76, 86.02, 42.91 uΩ, respectively. Compared with DC values, the AC values increase by 199%, 206%, and 198%, respectively. The DC and AC inductance of the three phases are 3.99, 5.75, 3.99 uΩ, and 3.53, 4.39, 3.53 uΩ, respectively. Compared with DC values, the AC values decreased by 12%, 24%, and

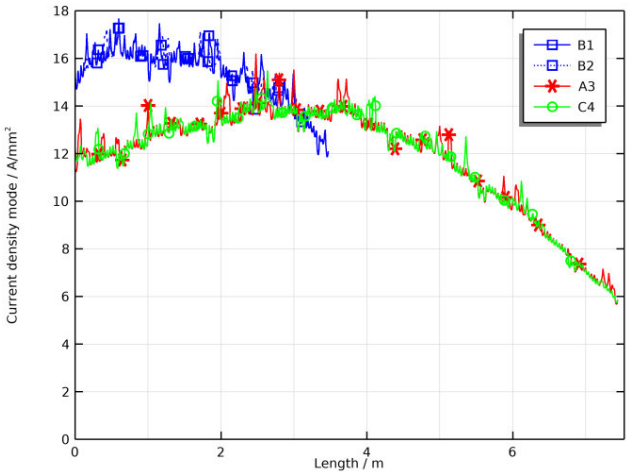

FIGURE 11. The current densities of the four cables with the high current densities.

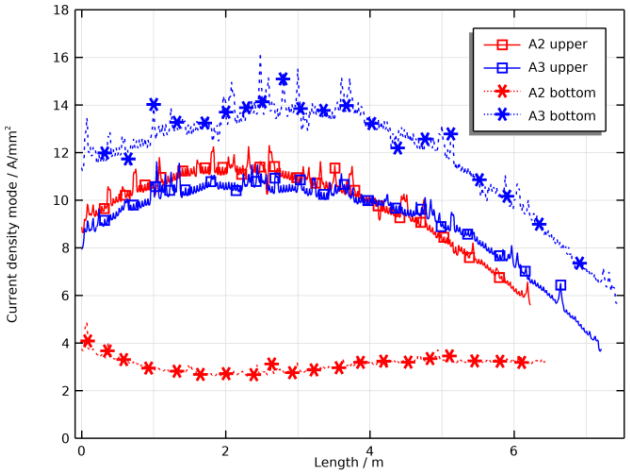

FIGURE 12. The current density at the upper and bottom of the curved part for cable A2 and A3.

12%, respectively. The AC reactance of the three phases is 1109.72, 1379.25, 1109.68 uΩ, respectively. The imbalance of the three-phase imbalance index is about 15%, mainly determined by inductance. The results indicate a significant difference in resistance between AC and DC, a relatively small difference in inductance, and a relatively low degree of three-phase impedance imbalance.

TABLE 2. The impedance of water-cooled cables.

	frequency/Hz	A-phase	B-phase	C-phase
resistance/uΩ	0	14.28	28.13	14.39
	50	42.76	86.02	42.91
inductance/uH	0	3.99	5.75	3.99
	50	3.53	4.39	3.53
reactance/uΩ	50	1109.72	1379.25	1109.68

C. CONDUCTIVE ARMS

The conductive arms are located in the third part of the short net system. The head end and tail end are connected with the water-cooled cables and the graphite electrodes, respectively. The conductor of phase A and C are geometrically symmetric. The tail end has small solid widgets, which are used to fix the graphite electrodes. The conductive arms are hollow conductors with a wall thickness of 1.5 cm and a geometric radius of 44 cm. The length is about 6.9 meters.

1) CURRENT DENSITY DISTRIBUTION

The surface current density of the conductive arms is given in Fig. 13. It can be seen that the maximum current density is 19.5 A/mm^2—the closer to the tail of the conductor, the higher the current density. The reason is similar to the copper bars in the first part of the short net system. The cross-section of the hollow conductors and the small solid widget are 183 cm^2 and 2940 cm^2, respectively. The difference in conductivity between the two is 15 times, resulting in the current density mutation occurring at the interface. The part with a small section has high current density and an extensive range of current density mutations. This situation also exists in the head end of the conductive arms, but the influence is relatively weak due to the short length of the small solid widget. Fig. 14 gives the current density distribution at x=10 m cross-section. Since the wall thickness of the conductor is minimal, the influence of the skin and proximity effect on current density is small. The radial current density at the edges and angle is uniform from the zooming figure.

Fig. 15 gives the current density along the x-axis. It can be seen that the current density of phases A and C changes in the same trend. The current density increases sharply at the conductor length of about 6.8 m, and the maximum current density is about 4.4 A/mm^2. The current density of phase B increases gradually from the beginning and sharply at the conductor length of about 6.3 m. The maximum current density reaches 6.8 A/mm^2. The sudden change of conductivity still causes an increase in current density. Overall, the current density of phase B is higher than the other two phases, which is related to the spatial position of the conductor. At the end area, three phase conductors are of the same horizontal height, affecting the current density of phase B significantly compared with the other two phases.

Fig. 16 shows the current density of the outer and inner walls for phase B—the current density of the outer and inner walls changes in the same trend. The maximum current density of the outer wall is 3 A/mm2, which is 1.9 times that of the inner wall. Although the analysis in Fig.11 shows that the skin effect is minimal, the skin effect still exists in Fig. 13, which is reflected in Fig. 14.

2) IMPEDANCE CALCULATION RESULTS

The impedance calculation results of the conductive arms are shown in Table 3. The DC and AC resistance of the three phases are 8.59, 8.97, 8.59 uΩ, and 13.63, 13.51, 13.63 uΩ, respectively. Compared with DC values, the AC values increase by 59%, 51%, and 59%, respectively. The DC and AC inductance of the three phases is 2.31, 1.75, 2.31 uΩ, and 2.22, 1.66, 2.22 uΩ, respectively. Compared with DC values, the AC values decrease by 4%, 5%, and

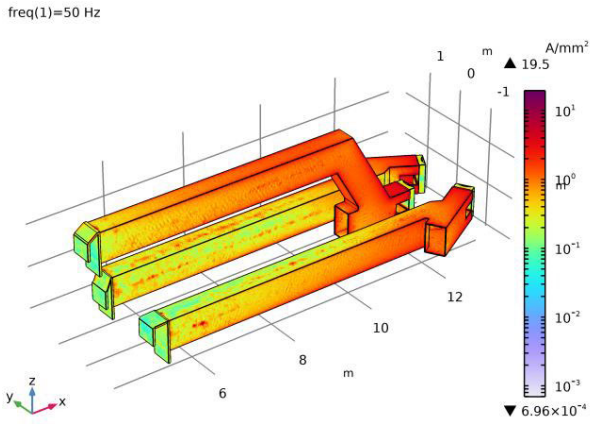

FIGURE 13. The surface current density of the conductive arms.

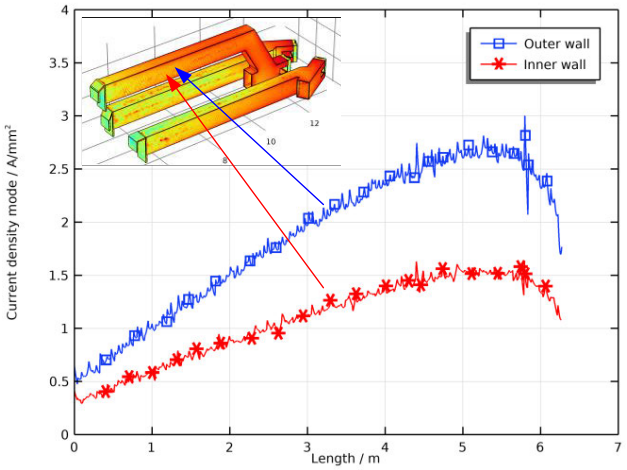

FIGURE 16. The current density of the outer and inner wall for phase B.

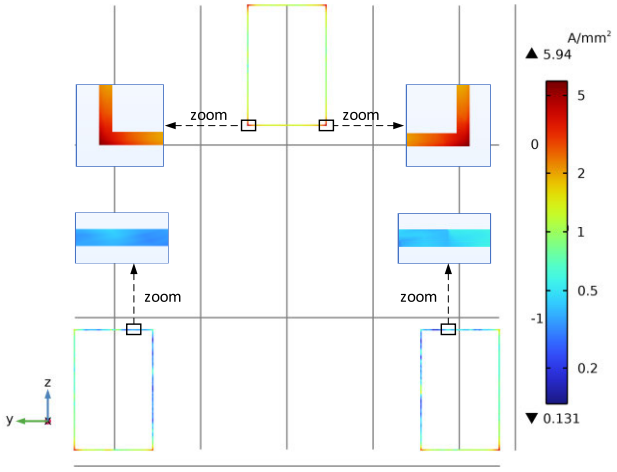

FIGURE 14. The current density at x=10 m cross section.

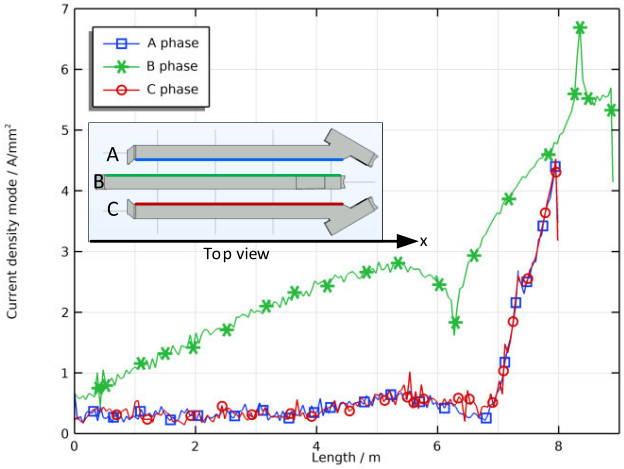

FIGURE 15. The current density along the x axis.

4%, respectively. The AC reactance of the three phases is 697.43, 521.55, 697.43 uΩ, respectively. The imbalance of the three-phase imbalance index is about 18%, mainly determined by inductance. The results indicate a relatively significant difference in resistance between AC and DC, a slight difference in inductance, and a relatively low degree of three-phase impedance imbalance.

TABLE 3. The impedance of the conductive arms.

	frequency/Hz	A-phase	B-phase	C-phase
resistance/uΩ	0	8.59	8.97	8.59
	50	13.63	13.51	13.63
inductance/uH	0	2.31	1.75	2.31
	50	2.22	1.66	2.22
reactance/uΩ	50	697.43	521.55	697.43

D. GRAPHITE ELECTRODES

The graphite electrodes are located at the end of the short net system. The head end is connected with the conductive arms, and the conductor of the three phases is geometrically symmetric. The length and radius of the graphite electrode are 9 m and 0.27 m, respectively.

1) CURRENT DENSITY DISTRIBUTION

The surface current density of the graphite electrodes is shown in Fig. 17. The current density of the electrode is not uniformly distributed in both radial and longitudinal directions. From the longitudinal point of view, the current density in the middle part is large, and the upper and lower ends are relatively small. The maximum current density is 0.362 A/mm2. Compared with the first three parts of the short net system, the current density of the graphite electrodes is small. The reason is that the conductivity of the graphite electrode is only 1/23,000 times that of copper, and the conductivity is proportional to the current density.

Fig. 18 gives the current density at the middle cross-section. It can be easily found that the skin and proximity effects significantly influence the radial current density distribution of graphite electrodes. Combined with Fig. 19, the distribution of the three-phase current density is symmetrical, and the amplitude is the same. The maximum current density occurs at the conductor length of 4.5 m, and the amplitude is

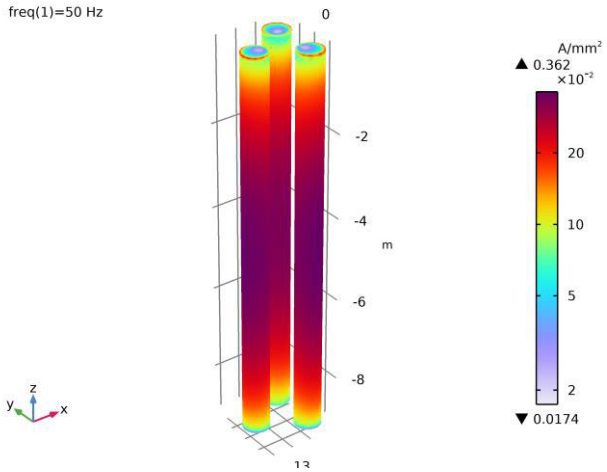

FIGURE 17. The surface current density of graphite electrodes.

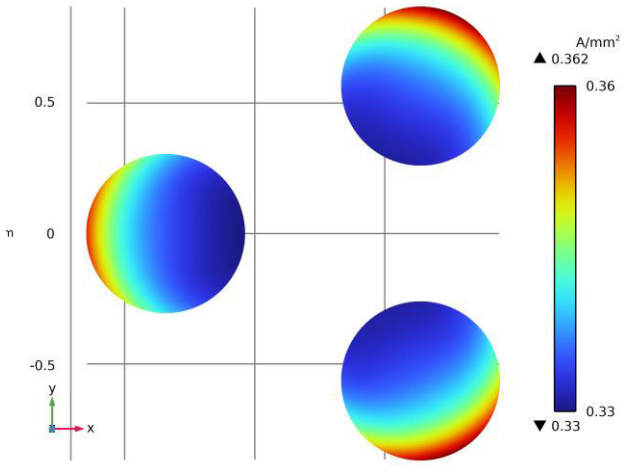

FIGURE 18. The current density at the middle cross section.

about 0.36 A/mm^2. From Fig. 20, the current density of the graphite electrode varies at the nearest and furthest distance from the pole center of the three-phase electrodes. The current density closer to the polar center is smaller, and farther away is more significant. The proximity effect seriously affects the graphite electrodes with a large radius and small spacing.

2) IMPEDANCE CALCULATION RESULTS

The impedance calculation results of the graphite electrodes are shown in Table 4. The DC and AC resistance of the three phases are 1306.01, 1306.01, 1306.01 uΩ, and 1327.36, 1328.13, 1327.35 uΩ, respectively. Compared with DC values, the AC values increase by 2%, 2%, and 2%, respectively. The DC and AC inductance of the three phases is 2.95, 2.76, 2.95 uΩ, and 2.94, 2.75, 2.94 uΩ, respectively. Compared with DC values, the AC values decrease by 0.3%, 0.4%, and 0.3%, respectively. The AC reactance of the three phases is 923.33, 864.59, 923.32 uΩ, respectively. The imbalance of the three-phase imbalance index is only about 1%, determined by resistance. The results indicate that the resistance and inductance of AC and DC are almost the same, and the three-phase impedance imbalance can be ignored.

TABLE 4. The impedance calculation results of graphite electrodes.

	frequency/Hz	A-phase	B-phase	C-phase
resistance/uΩ	0	1306.01	1306.01	1306.01
	50	1327.36	1328.13	1327.35
inductance/uH	0	2.95	2.76	2.95
	50	2.94	2.75	2.94
reactance/uΩ	50	923.33	864.59	923.32

E. COMPARISON WITH ANALYTICAL RESULTS

The comparison of the calculation results of different methods is shown in Table 5. Since analytical methods are not good at calculating conductors with complex geometric models, graphite electrodes are taken as the comparison object. AM1, AM2, and AM3 represent the three different analytical methods from [6], [22], and [23], respectively. AM1 focuses on correcting the DC resistance by the skin and proximity effect coefficient to obtain the AC resistance. The skin and proximity effect coefficients are $4.67 \times 10^{-5}$and 3.78×10^{-5}, respectively. Due to the low conductivity of the graphite

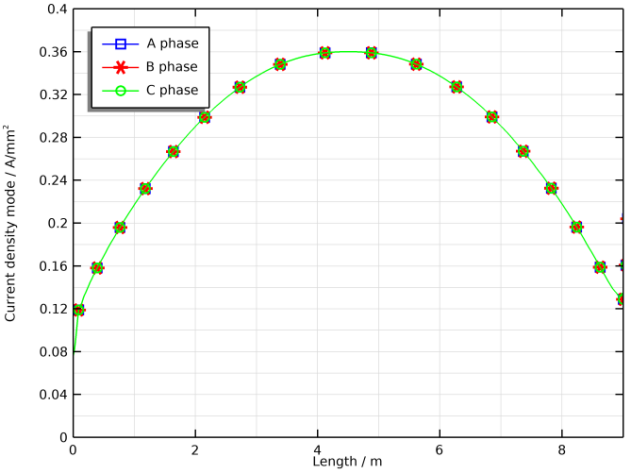

FIGURE 19. The outer edge current density for three phases.

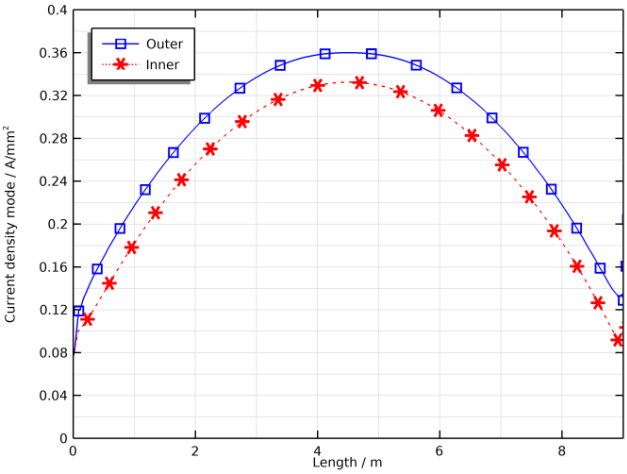

FIGURE 20. The outer and inner current density of graphite electrodes.

TABLE 5. The calculation results comparison of different methods.

		A-phase	B-phase	C-phase
resistance /uΩ	FEM	1327.36	1328.13	1327.35
	AM1	1327.53	1328.25	1327.52
	relative error	0.01%	0.01%	0.01%
inductance /uH	FEM	2.94	2.75	2.94
	AM2	2.41	2.41	2.41
	relative error	18.02%	12.37%	18.02%
self-inductance /uH	FEM	1.91	1.91	1.91
	AM3	1.92	1.92	1.92
	relative error	0.52%	0.52%	0.52%

electrodes, the two coefficients are very small. The relative error is about 0.01%, which reflects that the AC resistance difference between FEM and AM1 can be ignored. The second analytical method, AM2, pays attention to the GMD method. Since the skin and proximity effects of the conductor are ignored, the relative errors of inductance calculation results are significant relatively compared with FEM. The relative errors of the three phases are 18.02%, 12.37%, and 18.02%, respectively. Reference [23] fully considers the skin effect of conductors and proposes a method for calculating conductor self-inductance. Since the skin effect is considered, the relative error of the graphite electrodes' self-inductance based on FEM and AM3 is tiny. The relative errors of the three phases are 0.52%. Accordingly, the skin and proximity effect are both significant factors in conductor impedance calculation, and neglecting each factor will increase calculation error.

V. CONCLUSION

In order to calculate the impedance of short net conductors in electric heating systems of steel mills, this paper presents an impedance calculation method based on the FEM considering the skin and proximity effects. Firstly, a frequency domain electromagnetic field mathematical model of the short net conductor is established. Meanwhile, the corresponding boundary conditions are given. Further, the FEM based on the Galerkin weighted residual method is applied to discretize the established electromagnetic field model. The finite element calculation steps are given. Finally, a 100 t arc furnace short net system is an example. The current density distribution of different parts of the short net conductors is given and analyzed. Meanwhile, the DC and AC resistances are compared. The results are as follows:

(a) The impedance of each part of the short net conductors varies greatly. The AC resistance of copper tubes, water-cooled cables, and conductive arms exceeds the DC resistance greatly. The AC resistance of the first two exceeds the DC resistance by more than twice. The difference between the graphite electrodes can be ignored. The AC reactance is several tens of times higher than the resistance for copper tubes, water-cooled cables, and conductive arms. However, AC reactance is lower than resistance for graphite electrodes.

(b) The current density of the short net conductors is closely related to its geometry. A sudden change in the conductor cross-section can lead to a sharp increase in the current density of conductors with small cross-sections, which is evident in copper tubes and conductive arms.

(c) The three-phase impedance unbalance index of graphite electrodes is the smallest, and the index of copper tubes is the largest, followed by water-cooled cables and conductive arms.

Building on the insights from our research, we are excited to direct our future efforts toward optimizing the geometric parameters of the short net system to meet electrical requirements. We are also keen to explore the influence of temperature on impedance calculation results, which is a promising avenue for future research.

REFERENCES

[1] X. Wang, "Technological progress of EAF steelmaking in China," *Iron Steel*, vol. 54, no. 8, pp. 1–8, Oct. 2019.

[2] J. Suer, M. Traverso, and N. Jäger, "Review of life cycle assessments for steel and environmental analysis of future steel production scenarios," *Sustainability*, vol. 14, no. 21, p. 14131, Oct. 2022.

[3] I. H. Aziz, M. M. A. B. Abdullah, M. A. A. M. Salleh, L. Y. Ming, L. Y. Li, A. V. Sandu, P. Vizureanu, O. Nemes, and S. N. Mahdi, "Recent developments in steelmaking industry and potential alkali activated based steel waste: A comprehensive review," *Materials*, vol. 15, no. 5, p. 1948, Mar. 2022.

[4] P. Sarajč ev and R. Goić, "Power loss computation in high-current generator bus ducts of rectangular cross-section," *Electr. Power Compon. Syst.*, vol. 38, no. 13, pp. 1469–1485, Oct. 2010.

[5] I. A. Hernandez, J. M. Cañedo, J. C. Olivares-Galvan, and E. Betancourt, "Novel technique to compute the leakage reactance of three-phase power transformers," *IEEE Trans. Power Del.*, vol. 31, no. 2, pp. 437–444, Apr. 2016.

[6] X. Wan, S. Yang, Q. Li, and B. Li, "Time-varying inductance gradient in rails based on geometric mean distance," *IEEE Trans. Plasma Sci.*, vol. 51, no. 1, pp. 220–226, Jan. 2023.

[7] O. Coufal, "One hundred and fifty years of skin effect," *Appl. Sci.*, vol. 13, no. 22, p. 12416, Nov. 2023.

[8] M. Zareba, T. Szczegielniak, and P. Jabłonski, "Influence of the skin and proximity effects on the thermal field in a system of two parallel round conductors," *Energies*, vol. 16, no. 17, p. 6341, Sep. 2023.

[9] O. Gassab, H. Xie, Y. Chen, D.-E. Wen, S. Du, K. Luo, F. He, J. Meng, D. Zhao, D. Xiao, and W.-Y. Yin, "Fast and accurate semi-analytical solution to skin and proximity effects in shielded cable systems," *IEEE Trans. Electromagn. Compat.*, vol. 65, no. 6, pp. 1632–1646, Dec. 2023.

[10] O. Gassab, Y. Chen, Y. Shao, J. Li, D.-E. Wen, F. He, Z. Su, P. Zhong, J. Wang, D. Zhao, and W.-Y. Yin, "Accurate formulation of the skin and proximity effects in high-speed cable system," *IEEE Access*, vol. 10, pp. 100682–100699, 2022.

[11] G. Du, W. Ye, Y. Zhang, L. Wang, T. Pu, and N. Huang, "Comprehensive analysis of the AC copper loss for high speed PM machine with form-wound windings," *IEEE Access*, vol. 10, pp. 9036–9047, 2022.

[12] M. Zinelabiddine, A. Alzahrani, A. Alwabli, A. Jaffar, E. Ali, and M. S. Alzaidi, "Miniaturization and fabrication of a novel cross-fractal biosensor and sensor for characterizing 3D printing electromagnetic properties in polylactic acid," *IEEE Access*, vol. 12, pp. 33045–33056, 2024.

[13] I. N. Alquaydheb, S. A. Alfawaz, A. Ghadimi Avval, S. Ghayouraneh, and S. M. El-Ghazaly, "Modeling, characterization, and machine learning algorithm for rectangular choke horn antennas," *IEEE Access*, vol. 12, pp. 61697–61707, 2024.

[14] W.-C. Chang, C.-C. Kuo, W.-C. Lin, and M.-N. Hsieh, "Simulation of stray and core shielding loss for power transformer based on 2D/3D FEM," *IEEE Access*, vol. 11, pp. 16943–16950, 2023.

[15] H. Qiu, Z. Zhu, B. Xiong, and C. Yang, "Influence of eddy current loss on electromagnetic field and temperature field of high-speed permanent magnet generator with the toroidal windings," *IEEE Access*, vol. 10, pp. 98259–98267, 2022.

[16] A. A. Althuwayb, "The dilemma of resolving the low-frequency breakdown problem in microwave components via traditional and improved finite-element time-domain techniques," *IEEE Access*, vol. 10, pp. 42171–42180, 2022.

[17] A. Jamali-Abnavi and H. Hashemi-Dezaki, "Harmonic-based 3D thermal analysis of thyristor-controlled reactor's power cable joints considering external electromagnetic fields," *Electr. Power Syst. Res.*, vol. 205, Apr. 2022, Art. no. 107727.
[18] W. G. Shadid and R. Shadid, "Electric model for electromagnetic wave fields," *IEEE Access*, vol. 9, pp. 88782–88804, 2021.
[19] Z. Wang, Y. Si, and L. Liu, "Study on the induced geoelectric field of geomagnetic storm considering the underground anisotropic medium," *Trans. China Electrotechnical Soc.*, vol. 37, no. 5, pp. 1070–1077, Mar. 2022.
[20] Z. Wang, B. Dong, C. Liu, L. Liu, and L. Liu, "Three-dimensional earth conductivity structure modelling in north China and calculation of geoelectromagnetic fields during geomagnetic disturbances based on finite element method," *Trans. China Electrotechnical Soc.*, vol. 30, no. 3, pp. 61–66, Feb. 2015.
[21] Q. Liu, W. Wang, B. Fan, Q. Chen, and X. Zeng, "Voltage-type arc suppression method for an unbalanced distribution network considering the influence of line impedance and load," *Power Syst. Protection Control*, vol. 51, no. 7, pp. 24–31, Apr. 2023.
[22] Z. Xu and J. Qian, "Comparison of different methods for calculating electrical parameters of power cables," *High Voltage Eng.*, vol. 39, no. 3, pp. 689–697, Mar. 2013.
[23] X. Liu, L. Wang, G. Liang, and L. Qi, "Computing method for partial inductance of cylindrical busbar conductor," *Trans. China Electrotechnical Soc.*, vol. 35, no. 1, pp. 1–9, Jan. 2020.

QIAO MA (Member, IEEE) was born in 1991. He received the Ph.D. degree in engineering from Xi'an University of Technology, Xi'an, China, in 2023. He is currently a Post-Doctoral Fellow jointly trained by China National Heavy Machinery Research Institute Company Ltd., and Xi'an University of Technology. His research interests include finite element calculation and parameter optimization of electromagnetic fields in industrial electric heating systems.

BING TONG was born in 1969. She received the B.S. degree from Xidian University, Xi'an, China, in 1991, and the M.S. degree from Air Force Engineering University, Xi'an, in 2005. She is currently a Professor of engineering with China National Heavy Machinery Research Institute Company Ltd. She is the Chief Expert in electrical and intelligence with Sinomach Heavy Equipment Group Company Ltd. Her research interests include intelligent technology for refining equipment outside the furnace and adaptive control of arc furnace electrodes.

XIANGQIAN TONG was born in 1961. He received the B.S. degree from Shaanxi Institute of Technology, Hanzhong, China, in 1983, the M.S. degree from Xi'an University of Technology, Xi'an, China, in 1989, and the Ph.D. degree in electrical engineering from Xi'an Jiaotong University, Xi'an, in 2006. In 1989, he joined Xi'an University of Technology, where he has been a Professor and the Academic Leader in electrical engineering, since 2002. His research interest includes the application of power electronics in power systems.

TENG ZHAO was born in 1988. He received the M.S. degree from Hefei University of Technology, Hefei, China, in 2013. He is currently a Senior Engineer and the Director of the Institute of External Refining Equipment, China National Heavy Machinery Research Institute Company Ltd. His research interests include the development and application of vacuum refining equipment and vacuum acquisition equipment. He is the Vice Chairperson of Shaanxi Vacuum Society.

YADAN SHANG was born in 1982. She received the B.S. degree from Xi'an University of Science and Technology, Xi'an, China, in 2004. She is currently a Senior Engineer with China National Heavy Machinery Research Institute Company Ltd. Her research interest includes engineer optimization design of electric heating systems in steel mills.

FENGHUI ZHAO was born in 1977. He received the B.S. degree from Central South University, Changsha, China, in 2001. He is currently a Senior Engineer with China National Heavy Machinery Research Institute Company Ltd. His research interest includes engineer optimization design of electric heating systems in steel mills.

DONG ZHANG was born in 1979. He received the M.S. degree from Xi'an University of Science and Technology, Xi'an, China, in 2008. He is currently a Senior Engineer with China National Heavy Machinery Research Institute Company Ltd. His research interest includes engineer optimization design of electric heating systems in steel mills.